

# Deep Water Particle Paths in the Presence of Currents

C.W. Curtis<sup>1†</sup>, J.D. Carter<sup>2</sup> and H. Kalisch<sup>3</sup>

<sup>1</sup>Department of Mathematics and Statistics, San Diego State University, San Diego, CA 92182

<sup>2</sup>Mathematics Department, Seattle University, Seattle, WA 98122

<sup>3</sup>Department of Mathematics, University of Bergen, Bergen, Norway

(Received xx; revised xx; accepted xx)

The effect of constant vorticity background shear on the properties of wavetrains in deep water is investigated. Using the methodology of Fokas (2008), a nonlinear Schrödinger envelope equation is derived in the presence of background shear and surface tension, and the effects of the background shear on the modulational instability of plane waves is studied. These results complement the findings of Thomas *et al.* (2012).

Using a modification of the Generalized Lagrangian Mean theory Andrews & McIntyre (1978) and approximate formulas for the velocity field in the fluid column, it is found that background currents may have unexpected effects on the Stokes drift velocity. In particular, certain combinations of background shear and carrier frequency lead to the disappearance of the Lagrangian drift velocity. These results are in agreement with wave measurements reported in Smith (2006).

Explicit, asymptotic approximations for the Stokes drift velocity are obtained for plane wave and Jacobi elliptic function solutions of the nonlinear Schrödinger equation. Numerical approximations to particle trajectories for these solutions are found and the Stokes drift velocities and Lagrangian mean velocities corresponding to these numerical solutions corroborate the theoretical results. Our results also provide further evidence of the viability of the modification of the Stokes drift velocity beyond the standard monochromatic approximation, such as recently proposed in Breivik *et al.* (2014) in order to obtain a closer match to a range of complex ocean wave spectra.

## 1. Introduction

Currents are an ubiquitous feature in oceanic dynamics where they are a driving force in the formation and propagation of waves in the ocean. Currents in shallow water over bathymetric variations are a key mechanism for surface and internal wave generation Helfrich & Melville (2006). In deep water, slowly varying currents act as refractive medium for small amplitude, linear surface-water waves Gallet & Young (2014). While the impact of slowly varying currents on deep water small amplitude surface waves has been extensively studied, what is less well understood is the impact of more rapidly varying currents, and in particular, their effect on larger amplitude nonlinear surface waves.

A simple case of such a current is that of a constant vorticity shear current, which has been studied in Brevik (1979); Simmen & Saffman (1985); Baumstein (1998); Choi (2009); Thomas *et al.* (2012). In particular, in Thomas *et al.* (2012) the impact of vorticity on the modulational instabilities (MIs) of wave trains in deep water was examined. The MI, which is also known as the Benjamin–Feir instability, is a key factor in the understanding

† Email address for correspondence: ccurtis@mail.sdsu.edu

of a number of wave phenomena, and it is particularly important in the study of issues such as wave breaking and freak wave formation. In Thomas *et al.* (2012) it is shown that constant vorticity strongly modifies the onset and bandwidth of MIs. Further, it is shown that some currents can even completely suppress MIs, which is a striking result and speaks to the importance of better understanding the role of shear currents in deep water flows.

What is less well known is how currents impact the transport properties of surface waves. A key measure of the strength of the material transport of surface waves is the Stokes drift velocity (SDV), which in the absence of background currents is the mean speed at which fluid parcels travel in a flow Longuet-Higgins (1953). An understanding of the SDV is critical in understanding the transport of material and energy in oceanic environments, and it has been a subject of considerable interest Breivik *et al.* (2014); McWilliams *et al.* (1997); Webb & Fox-Kemper (2011). Regarding the impact of constant vorticity currents on the transport properties of surface waves in deep water, the experimental work of Monismith *et al.* (2007) and the field measurements of Smith (2006) seem to suggest wavetrains on deep water excite Eulerian counter currents which in effect cancel the mean flow induced by the SDV. These counter currents cancel surface drift in the open ocean Smith (2006) and drift at both the surface and throughout the bulk of fluids in laboratory settings Monismith *et al.* (2007). To date, there seems to be no theoretical framework explaining the mechanisms behind the development of these currents.

A different but related dilemma emerges in attempts to fit classic, current free, derivations for the SDV in deep water to oceanographic data. In recent work Breivik *et al.* (2014), the authors put forward phenomenological modifications to the SDV profile which amount to introducing background currents. As the authors show, the use of these modified SDV profiles is superior to the standard approach of using monochromatic SDV profiles. However, no physical mechanism is provided which explains the origins of the modifications used in Breivik *et al.* (2014).

In order then to better understand the impact of constant vorticity, and thus background shear currents, on deep water surface flows, we study how a constant vorticity shear profile influences the motion and mean properties of particle paths generated by waves in infinitely deep water. Our analysis complements the shallow and finite depth results found in Constantin (2011); Borluk & Kalisch (2012) and it expands on the numerical results in Jr *et al.* (2017). We first derive a nonlinear Schrödinger (NLS) model to describe the impact of constant vorticity via the methodology of Ablowitz–Fokas–Musslimani (AFM) Ablowitz *et al.* (2006); Ashton & Fokas (2011), which is a particular case of the more general approach of the Unified Transform Method Fokas (2008). Using this derivation, we determine not only the appropriate form of the NLS equation, but also the mean-surface height and tangential-surface velocity. We show that the mean-surface height is markedly increased due to the background shear current. We characterize the impact of constant vorticity on MIs, complementing the results in Thomas *et al.* (2012). We note that our derivation method is quite distinct from that in Thomas *et al.* (2012) and provides yet another example of the utility of the AFM formulation. We then derive dynamical systems which describe the particle paths.

Using the above derivations, we provide the first description of the impact of constant vorticity shear currents on the SDV via the techniques of the Generalized Lagrangian Mean (GLM) theory Andrews & McIntyre (1978); Bühler (2009). This approach provides an unambiguous way of computing the SDV under the influence of depth varying currents, whereby we are then able to explicitly derive formulas for the SDV for a wide variety of solutions to the NLS equation. Our method enables us to quantify the combined

effect of background shear and wave modulation, and to determine which combinations of background shear and carrier wave frequency produce particularly strong or weak mean flows. Further, we are able to show which background shear currents quench mean surface flows, thereby providing a potential theoretical explanation for the results seen in Smith (2006). We also show how one can derive from our model the phenomenological modifications used in Breivik *et al.* (2014).

As will come to light in the body of the paper, in order to accurately predict which background shear current is able to reduce or remove any mean surface flow, a slight extension of the standard GLM theory is needed. While this generalization is relatively straightforward, it does introduce the interesting question of how to adapt the GLM framework to more general fluid problems with strong background current flows, and thus opens up a number of future research topics.

As a way of confirming our theoretical findings, we discretize the dynamical system describing particle trajectories in the NLS approximation and compute numerical approximations of such trajectories. Our numerical results show that the impact of background shear currents on particle paths and the SDV are in line with the results predicted by our theory. We generate the numerical approximations by using the Jacobi elliptic function solutions for both the focusing and defocusing NLS equations to model deep water time-evolving surface waves. Complementing these results, we also examine the defocusing plane-wave solutions of the NLS equation. Our results show how transport properties are most enhanced for shear currents which propagate at the surface against the carrier wave. This can occur near what appear to be resonances between nonlinearity and the background shear profile. Likewise, in the defocusing case we numerically confirm the theoretical predictions made for those balances between vorticity and carrier wave-number which one expects to quench the mean surface drift, , thereby providing a possible explanatory mechanism for the results in Smith (2006); Breivik *et al.* (2014); Monismith *et al.* (2007). In total, our theoretical and numerical results show that the transport properties of surface waves can be deeply affected by constant vorticity background shear profiles and motivating further study of the impact of rapidly depth-varying currents.

The outline of the paper is as follows. The derivations of the NLS equation and the dynamical system describing particle paths is given in Section 2. The explanations and derivations of the formulas necessary to compute the Stokes drift velocity are given in Section 3. The numerical results on the particle paths and Stokes drift velocity are in Section 4.

## 2. Derivations

### 2.1. Derivation of NLS with Constant Vorticity in Infinite Depth

We examine the unsteady nonlinear wave propagation over a constant shear current. To do this, we assume the fluid velocity has the form

$$\mathbf{u} = u(\mathbf{x}, t)\hat{\mathbf{x}} + w(\mathbf{x}, t)\hat{\mathbf{z}} = \omega z\hat{\mathbf{x}} + \nabla\phi,$$

where  $\phi$  is a harmonic function. We restrict fluid motion to the  $(x, z)$ -plane, thereby ignoring transverse variations in the  $y$  dimension. Following standard arguments, e.g. see Ashton & Fokas (2011), the dynamics of the fluid can be determined by solving the free

boundary value problem

$$\begin{aligned} \Delta\phi &= 0, & -\infty < z < \eta(x, t), \\ \eta_t + (\omega\eta + \phi_x)\eta_x - \phi_z &= 0, & z = \eta(x, t), \end{aligned} \quad (2.1)$$

$$\begin{aligned} \phi_t + \omega\partial_x^{-1}\eta_t + \frac{1}{2}|\mathbf{u}|^2 + g\eta - \frac{\sigma}{\rho}\partial_x\frac{\eta_x}{\sqrt{1+\eta_x^2}} &= 0, & z = \eta(x, t), \\ \lim_{z \rightarrow -\infty} \phi_z &= 0. \end{aligned} \quad (2.2)$$

where  $\eta$  represents the free surface displacement, and  $g$ ,  $\rho$ , and  $\sigma$  represent the acceleration due to gravity, the fluid density, and the coefficient of surface tension respectively.

By choosing a characteristic wave height  $a$  and wave length  $L$ , all quantities can be non-dimensionalized via

$$\begin{aligned} \tilde{x} &= \frac{x}{L}, \quad \tilde{z} = \frac{z}{L}, \quad \tilde{t} = \sqrt{\frac{g}{L}} t, \quad \omega = \sqrt{\frac{g}{L}} \tilde{\omega}, \\ \eta &= a\tilde{\eta}, \quad \phi = a\sqrt{gL}\tilde{\phi}, \quad \epsilon = \frac{a}{L}. \end{aligned}$$

By following the AFM approach described in Ablowitz *et al.* (2006); Ashton & Fokas (2011) and dropping the tildes, the kinematic boundary condition, Equation (2.1), can be written in terms of surface variables alone via the integro-differential equation

$$\int_{\mathbb{R}} dx e^{-ikx} e^{\epsilon|k|\eta} (\eta_t + \epsilon\omega\eta\eta_x + i\text{sgn}(k)Q) = 0, \quad k \neq 0, \quad (2.3)$$

where  $Q = q_x$ ,  $q(x, t) = \phi(x, \eta(x, t), t)$ . By integrating over  $\mathbb{R}$ , we are assuming that both  $\eta$  and  $Q$  decay to zero amplitude in the far field. We can also readily derive a nearly identical expression on domains periodic in the horizontal variable  $x$ , in which case Equation (2.5) becomes, assuming a spatial period of  $L_p$ ,

$$\int_{-L_p/2}^{L_p/2} dx e^{-ikx} e^{\epsilon|k|\eta} (\eta_t + \epsilon\omega\eta\eta_x + i\text{sgn}(k)Q) = 0, \quad k = \frac{2\pi m}{L_p}, \quad m \in \mathbb{Z} \setminus 0. \quad (2.4)$$

Throughout the remainder of this section we only present results over the real line  $\mathbb{R}$  since identical results can be derived in the periodic case. Taylor expanding Equation (2.3) up to  $\mathcal{O}(\epsilon^2)$  for  $k \neq 0$  gives

$$\int_{\mathbb{R}} dx e^{-ikx} \left( 1 + \epsilon|k|\eta + \frac{\epsilon^2|k|^2\eta^2}{2} \right) (\eta_t + i\text{sgn}(k)Q) + \epsilon\omega \int_{\mathbb{R}} dx e^{-ikx} (1 + \epsilon|k|\eta) \eta\eta_x = 0. \quad (2.5)$$

Transforming into surface variables and Taylor expanding Equation (2.2), Bernoulli's equation, up to  $\mathcal{O}(\epsilon^2)$  gives

$$Q_t + \omega\eta_t + \eta_x - \tilde{\sigma}\eta_{xxx} + \frac{\epsilon}{2}\partial_x(-\eta_t^2 + (Q + \omega\eta)^2) + \epsilon^2\partial_x\left(\frac{3}{2}\tilde{\sigma}\eta_x^2\eta_{xx} - \eta_t\eta_x(Q + \omega\eta)\right) = 0,$$

where the Bond number  $\tilde{\sigma}$  is given by

$$\tilde{\sigma} = \frac{\sigma}{\rho g L^2}.$$

We note that we have tacitly assumed  $\omega = \mathcal{O}(1)$ . In physical terms, this implies that  $\omega$  is comparable to the natural time scale of this problem,  $\sqrt{g/L}$ . If we were to assume  $\omega$  were of larger magnitude, the problem would no longer be weakly nonlinear and thus would be much less amenable to asymptotic analysis. Therefore, throughout the remainder of the paper, we assume that the vorticity is not too large.

The nonlocality in the full equations comes from the Hilbert transform,  $\mathcal{H}$ , defined by

$$\mathcal{H}f = \frac{1}{2\pi} \int_{\mathbb{R}} dk e^{ikx} i \operatorname{sgn}(k) \hat{f}(k),$$

where  $\hat{f}(k)$  is the Fourier transform of  $f(x)$  defined by

$$\hat{f}(k) = \int_{\mathbb{R}} dx e^{-ikx} f(x).$$

In other words,  $\mathcal{H}$  is the operator with symbol  $i \operatorname{sgn}(k)$ . Given that

$$\operatorname{sgn}(k_0 + \epsilon k) = \operatorname{sgn}(k_0) \operatorname{sgn} \left( 1 + \frac{\epsilon k}{k_0} \right),$$

assuming  $\hat{f}(k)$  is a function of rapid decay Folland (1999), and assuming  $k_0 \gg \epsilon$  gives

$$\begin{aligned} \mathcal{H}(f(\epsilon x) e^{ik_0 x}) &= \frac{e^{ik_0 x}}{2\pi} \int_{\mathbb{R}} dk e^{ik\epsilon x} i \operatorname{sgn}(k_0 + \epsilon k) \hat{f}(k) \\ &\sim i \operatorname{sgn}(k_0) e^{ik_0 x} f(\epsilon x). \end{aligned}$$

with the difference being exponentially small. On the other hand, if  $k_0 = 0$ , then

$$\mathcal{H}(f(\epsilon x)) = \frac{1}{2\pi} \int_{\mathbb{R}} dk e^{ik\epsilon x} i \operatorname{sgn}(k) \hat{f}(k) = (\mathcal{H}f)(\epsilon x).$$

Thus, the Hilbert transform does not have any significant effect on the multiple scales ansätze made below.

Equation (2.5) can be rewritten as

$$\eta_t + \mathcal{H}Q + \epsilon \partial_x \left( Q\eta + \frac{\omega}{2} \eta^2 - \frac{1}{2} \mathcal{H} \partial_t \eta^2 \right) - \epsilon^2 \partial_x^2 \left( \frac{1}{6} \partial_t \eta^3 + \frac{\omega}{3} \mathcal{H} \eta^3 + \frac{1}{2} \mathcal{H}(\eta^2 Q) \right) = 0.$$

Using the expansions

$$\begin{aligned} \eta(x, t) &= \tilde{\eta}(x, X, t, T, \tau) + \mathcal{O}(\epsilon^3), \\ Q(x, t) &= \tilde{Q}(x, X, t, T, \tau) + \mathcal{O}(\epsilon^3), \end{aligned}$$

where

$$\tilde{\eta}(x, X, t, T, \tau) = \epsilon \eta_0(X, T, \tau) + \eta_1(X, T, \tau) e^{i\theta(x, t)} + \epsilon \eta_2(X, T, \tau) e^{2i\theta(x, t)} + \text{c.c.}, \quad (2.6)$$

$$\tilde{Q}(x, X, t, T, \tau) = \epsilon^2 q_0(X, T, \tau) + q_1(X, T, \tau) e^{i\theta(x, t)} + \epsilon q_2(X, T, \tau) e^{2i\theta(x, t)} + \text{c.c.}, \quad (2.7)$$

$$\theta(x, t) = k_0 x + \Omega(k_0, \omega) t, \quad X = \epsilon x, \quad T = \epsilon t, \quad \tau = \epsilon^2 t,$$

and expanding and matching harmonics and powers of  $\epsilon$  gives the linear dispersion relation,

$$\Omega_{\pm}(k_0, \omega) = \frac{1}{2} \left( s\omega \pm \sqrt{\omega^2 + 4|k_0|(1 + \tilde{\sigma} k_0^2)} \right), \quad (2.8)$$

at  $\mathcal{O}(1)$ . At  $\mathcal{O}(\epsilon)$ , the expansions give

$$\begin{aligned} \eta_2 &= \frac{k_0(2\omega\Omega + 2s^2\omega\Omega - s(\omega^2 + 2\Omega^2))}{2(k_0s + 4k_0^3s\tilde{\sigma} + (s\omega - 2\Omega)\Omega)} \eta_1^2 \\ q_2 &= \frac{-k_0(k_0\omega + 4k_0^3\tilde{\sigma}\omega + 2(s\omega - \Omega)\Omega^2)}{k_0s + 4k_0^3s\tilde{\sigma} + (s\omega - 2\Omega)\Omega} \eta_1^2 \end{aligned}$$

and the linear advection equation

$$\partial_T \eta_1 - c_g \partial_X \eta_1 = 0, \quad c_g(k_0, \omega) = \frac{1 + 3\tilde{\sigma}k_0^2}{2s\Omega - \omega},$$

where  $s = \text{sgn}(k_0)$ . Introducing the new coordinate

$$\xi = X + c_g T,$$

and solving at  $\mathcal{O}(\epsilon^2)$  defines the mean terms

$$\eta_0 = \frac{\omega(2\Omega s - \omega)}{1 + c_g \omega} |\eta_1|^2, \quad (2.9)$$

$$q_0 = \frac{(\omega - 2s\Omega)}{1 + c_g \omega} \mathcal{H} \partial_\xi |\eta_1|^2, \quad (2.10)$$

and the NLS equation for a constant shear flow on an infinitely deep fluid

$$i\partial_\tau \eta_1 + \alpha_{nl} |\eta_1|^2 \eta_1 + \alpha_d \partial_\xi^2 \eta_1 = 0,$$

where

$$\alpha_d(k_0, \omega) = \frac{(c_g^2 - 3|k_0|\tilde{\sigma})}{2\Omega - s\omega},$$

$$\alpha_{nl}(k_0, \omega) = \frac{k_0 (sk_0^3 (8 + \tilde{\sigma}k_0^2 + 2(\tilde{\sigma}k_0^2)^2) + \omega\alpha_v)}{(2s\Omega - \omega)(1 + c_g\omega)(4\Omega^2 - s(2k_0(1 + 4\tilde{\sigma}k_0^2) + 2\omega\Omega))},$$

and

$$\begin{aligned} \alpha_v(k_0, \omega) = & s(c_g k_0 - 2\Omega)\omega^4 + k_0(4k_0^2 s\tilde{\sigma} + 2\Omega c_g - s)\omega^3 \\ & + k_0(16c_g k_0^3 \tilde{\sigma} - 8\Omega k_0^2 \tilde{\sigma} + 10c_g k_0 - 6\Omega)\omega^2 \\ & - k_0^2(15\Omega c_g k_0^2 s\tilde{\sigma} - 16k_0^4 \tilde{\sigma}^2 - 24k_0^2 \tilde{\sigma} - 2)\omega \\ & + k_0^3(2c_g k_0^4 s\tilde{\sigma}^2 + c_g k_0^2 s\tilde{\sigma} - 15\Omega k_0 s\tilde{\sigma} + 8c_g s). \end{aligned}$$

The case in which  $\alpha_d$  and  $\alpha_{nl}$  have the same sign is known as the ‘focusing’ case while the case in which they have opposite signs is known as the ‘defocusing’ case. These two cases are qualitatively different. In the focusing case, the trivial-phase Jacobi elliptic solutions are given by

$$\eta_1(\xi, \tau) = \kappa \beta \sqrt{\frac{2\alpha_d}{\alpha_{nl}}} \text{cn}(\beta\xi; \kappa) e^{-i\alpha_d \beta^2 (1 - 2\kappa^2)\tau}, \quad (2.11)$$

where  $0 \leq \kappa \leq 1$  is the elliptic modulus. In the  $\kappa \rightarrow 1$  limit, these solutions limit to the ‘bright’ soliton solutions

$$\eta_1(\xi, \tau) \rightarrow \beta \sqrt{\frac{2\alpha_d}{\alpha_{nl}}} \text{sech}(\beta\xi) e^{i\alpha_d \beta^2 \tau}.$$

In the defocusing case, the trivial-phase Jacobi elliptic solutions are given by

$$\eta_1(\xi, \tau) = \kappa \beta \sqrt{-\frac{2\alpha_d}{\alpha_{nl}}} \text{sn}(\beta\xi; \kappa) e^{-i\alpha_d \beta^2 (1 + \kappa^2)\tau}. \quad (2.12)$$

In the  $\kappa \rightarrow 1$  limit, these solutions limit to the ‘dark’ soliton solutions

$$\eta_1(\xi, \tau) \rightarrow \beta \sqrt{-\frac{2\alpha_d}{\alpha_{nl}}} \tanh(\beta\xi) e^{-2i\alpha_d \beta^2 \tau}.$$

The elevated profile of the magnitude of the bright soliton is qualitatively different from

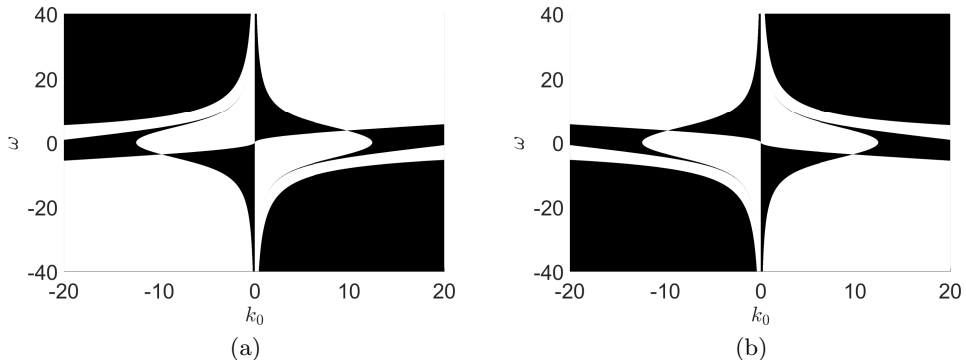


FIGURE 1. *MIs exist* - white, *MIs suppressed* - black, for  $\Omega_+(k_0, \omega)$  (a) and  $\Omega_-(k_0, \omega)$  (b).

the depressed profile of the magnitude of the dark soliton. This distinction typifies the difference between the behavior of the focusing and defocusing cases. Note that in order to have periodic boundary conditions when Jacobi elliptic functions are used, the following restriction must be enforced

$$k_0 = \frac{\pi \epsilon m}{2K(\kappa)}, \quad m \in \mathbb{Z}, \quad (2.13)$$

where  $K(\kappa)$  is the complete elliptic integral of the first kind.

## 2.2. Modulational Instabilities and Currents in Infinite Depth

The plane-wave, or Stokes wave, solutions of the NLS equation are given by

$$\eta_1(\xi, \tau) = A e^{i\alpha_{nl} A^2 \tau}, \quad (2.14)$$

where  $A > 0$  is a real constant. Complementing the results in Thomas *et al.* (2012), we study the stability of these solutions by considering perturbed solutions of the form

$$\eta_{1p}(\xi, \tau) = \left( A + \mu(u_p(\xi, \tau) + i v_p(\xi, \tau)) + \mathcal{O}(\mu^2) \right) e^{i\alpha_{nl} A^2 \tau}, \quad (2.15)$$

where  $\mu$  is a small real parameter and  $u_p$  and  $v_p$  are real-valued functions. Substituting (2.15) into the NLS equation and linearizing gives

$$\partial_\tau \begin{pmatrix} u_p \\ v_p \end{pmatrix} = \begin{pmatrix} 0 & -\alpha_d \partial_\xi^2 \\ \alpha_d \partial_\xi^2 + 2A^2 \alpha_{nl} & 0 \end{pmatrix} \begin{pmatrix} u_p \\ v_p \end{pmatrix}.$$

Separating variables, applying a Fourier transform in  $\xi$ , and introducing the  $\xi$  wave number  $l$ , establishes that NLS plane-wave solutions are unstable with respect to the modulational instabilities (MIs) if

$$0 < l^2 \leq 2 \frac{\alpha_{nl}}{\alpha_d} A^2.$$

This reduces to the classic requirement that MIs are suppressed if the coefficients of dispersion and nonlinearity have opposite signs (i.e. the defocusing case).

Figure 1 shows the values of  $\omega$  and  $k_0$  for which MIs exist (white areas) or not (black areas) for  $\tilde{\sigma} = 10^{-3}$ . We use this value for surface tension for the remainder of this paper. There does not appear to be a value of  $\omega$  that suppresses MIs across all wave numbers. Note that this does not contradict the results in Thomas *et al.* (2012) since we are considering both positive and negative values of  $k_0$ .

Per our convention of taking the fast phase,  $\theta(x, t)$ , to be

$$\theta(x, t) = k_0 x + \Omega(k_0, \omega)t,$$

if  $k_0 > 0$  and  $\Omega(k_0, \omega) > 0$ , then the carrier wave propagates to the left, while if  $k_0 > 0$  and  $\Omega(k_0, \omega) < 0$ , it is propagating to the right. These relationships are reversed if  $k_0 < 0$ . We note that Equation (2.8) establishes that  $\Omega_+(k_0, \omega) > 0$  and  $\Omega_-(k_0, \omega) < 0$  for  $k_0 \neq 0$ . Figures 1(a) and (b) then show that MIs are generally suppressed when the shear current at the surface is co-propagating with respect to the carrier wave with sufficient strength which is inversely related to the carrier wavenumber. Thus, in order to suppress most MIs, we need either relatively high carrier wave numbers  $k_0$  for relatively weak shear currents, or relatively strong shear currents for relatively low carrier wave numbers. The regions in Figures 1(a) and (b) in which counter-propagating sheer currents suppress MIs are more complicated in nature, though one can argue that counter-propagating currents generally exacerbate MIs, especially with increasing shear strength.

### 2.3. Derivation of Velocity Formulas

In non-dimensional coordinates, the position of a given fluid particle,  $(x(t), z(t))$ , is defined by the dynamical system

$$\begin{aligned} \dot{x} &= \omega z + \epsilon \phi_x(x, z, t), & \dot{z} &= \epsilon \phi_z(x, z, t), \\ x(0) &= x_0, & z(0) &= z_0. \end{aligned} \quad (2.16)$$

Therefore, in order to track the motion of a fluid particle, both  $\phi_x$  and  $\phi_z$  must be known throughout the fluid domain. In order to determine asymptotic formulas for these quantities, let

$$\phi_x(x, z, t) = \frac{1}{2\pi} \int_{\mathbb{R}} dk e^{ikx} A(k, t) e^{|k|z}, \quad (2.17)$$

$$\phi_z(x, z, t) = \frac{1}{2\pi} \int_{\mathbb{R}} dk e^{ikx} B(k, t) e^{|k|z}. \quad (2.18)$$

Expanding  $e^{\epsilon\eta|k|}$  in Equations (2.17) and (2.18) gives

$$\phi_x|_{z=\epsilon\eta} = \tilde{A}(x, t) - \epsilon\eta \mathcal{H} \partial_x \tilde{A} + \mathcal{O}(\epsilon^2), \quad (2.19)$$

$$\phi_z|_{z=\epsilon\eta} = \tilde{B}(x, t) - \epsilon\eta \mathcal{H} \partial_x \tilde{B} + \mathcal{O}(\epsilon^2), \quad (2.20)$$

where

$$\tilde{A}(x, t) = \frac{1}{2\pi} \int_{\mathbb{R}} dk e^{ikx} A(k, t), \quad \tilde{B}(x, t) = \frac{1}{2\pi} \int_{\mathbb{R}} dk e^{ikx} B(k, t).$$

The surface boundary conditions give

$$\begin{aligned} \phi_x|_{z=\epsilon\eta} &= \frac{Q - \epsilon\eta_x(\eta_t + \epsilon\omega\eta\eta_x)}{1 + \epsilon^2\eta_x^2}, \\ \phi_z|_{z=\epsilon\eta} &= \frac{\eta_t + \epsilon(Q + \omega\eta)\eta_x}{1 + \epsilon^2\eta_x^2}. \end{aligned}$$

Substituting the expansions in Equations (2.6) and (2.7) into these equations and using the results obtained during the derivation of the NLS equation gives

$$\begin{aligned} \phi_x|_{z=\epsilon\eta} &= -2\epsilon k_0 \Omega |\eta_1|^2 + (-s\Omega\eta_1 + i\epsilon s c_g \partial_\xi \eta_1) e^{i\theta} \\ &\quad - \epsilon(2s\Omega\eta_2 + k_0(s\omega - \Omega)\eta_1^2) e^{2i\theta} + \text{c.c.} + \mathcal{O}(\epsilon^2), \end{aligned} \quad (2.21)$$

$$\phi_z|_{z=\epsilon\eta} = (i\Omega\eta_1 + \epsilon c_g \partial_\xi \eta_1) e^{i\theta} + i\epsilon(2\Omega\eta_2 + k_0(\omega - s\Omega)\eta_1^2) e^{2i\theta} + \text{c.c.} + \mathcal{O}(\epsilon^2). \quad (2.22)$$



This motivates the expansions

$$\begin{aligned}\tilde{A}(x, t) &= \epsilon \tilde{A}_{01}(\xi, \tau) + \left( \tilde{A}_{10}(\xi, \tau) + \epsilon \tilde{A}_{11}(\xi, \tau) \right) e^{i\theta(x, t)} + \epsilon \tilde{A}_{21}(\xi, \tau) e^{2i\theta(x, t)} + \text{c.c.} + \mathcal{O}(\epsilon^2), \\ \tilde{B}(x, t) &= \epsilon \tilde{B}_{01}(\xi, \tau) + \left( \tilde{B}_{10}(\xi, \tau) + \epsilon \tilde{B}_{11}(\xi, \tau) \right) e^{i\theta(x, t)} + \epsilon \tilde{B}_{21}(\xi, \tau) e^{2i\theta(x, t)} + \text{c.c.} + \mathcal{O}(\epsilon^2).\end{aligned}$$

Inserting these expansions into Equations (2.19) and (2.20) and matching powers of  $\epsilon$  with the expansions in Equations (2.21) and (2.22) gives

$$\begin{aligned}\tilde{A}_{01} &= 0, \\ \tilde{A}_{10} &= -s\Omega\eta_1, \\ \tilde{A}_{11} &= isc_g \partial_\xi \eta_1, \\ \tilde{A}_{21} &= -(2s\Omega\eta_2 + k_0(s\omega - 2\Omega)\eta_1^2).\end{aligned}$$

The expressions for the corresponding terms in  $\tilde{B}$  can be found in a similar manner.

Inverting the Fourier transforms leads to expressions for  $A(k, t)$  and  $B(k, t)$ , which when inserted back into Equations (2.17) and (2.18) gives

$$\phi_x(x, z, t) = \tilde{\phi}_x(x, z, t) + \mathcal{O}(\epsilon^2), \quad \phi_z(x, z, t) = \tilde{\phi}_z(x, z, t) + \mathcal{O}(\epsilon^2),$$

where

$$\tilde{\phi}_x(x, z, t) = R_1(\xi, z, \tau) e^{i\theta} + \epsilon R_2(\xi, z, \tau) e^{2i\theta} + \text{c.c.}, \quad (2.23)$$

$$\tilde{\phi}_z(x, z, t) = \tilde{R}_1(\xi, z, \tau) e^{i\theta} + \epsilon \tilde{R}_2(\xi, z, \tau) e^{2i\theta} + \text{c.c.} \quad (2.24)$$

Again, while the expansion procedure is straightforward, due to the length of the expressions involved, the details have been omitted. However, we can still obtain approximations that will be useful later in this paper. In particular, the leading order behaviors of  $R_1$  and  $\tilde{R}_1$ , which in turn gives the leading order behaviors of the velocity potentials, are given by

$$R_1(\xi, z, \tau) \sim -\frac{s\Omega}{2\pi} \int_{\mathbb{R}} dk \, e^{ik\xi} e^{|k_0 + \epsilon k|z} \hat{\eta}_1(k, \tau), \quad (2.25)$$

$$\tilde{R}_1(\xi, z, \tau) \sim \frac{i\Omega}{2\pi} \int_{\mathbb{R}} dk \, e^{ik\xi} e^{|k_0 + \epsilon k|z} \hat{\eta}_1(k, \tau). \quad (2.26)$$

### 3. The Stokes Drift Velocity

We now show how our above approximation schemes can be used in to determine how a background shear current modifies the Stokes drift velocity (SDV). Following the Generalized Lagrangian Mean (GLM) formalism presented in Andrews & McIntyre (1978), for some quantity  $\varphi(\mathbf{x}, t)$ , given an Eulerian mean operator  $(\bar{\cdot})$ , we define the Lagrangian mean  $(\bar{\cdot})^L$  at a point  $\mathbf{x}$  relative to the disturbance  $\mathbf{y}(\mathbf{x}, t)$  to be

$$\bar{\varphi}^L(\mathbf{x}, t) = \overline{\varphi(\mathbf{x} + \mathbf{y}(\mathbf{x}, t), t)}.$$

See Kundu *et al.* (2012) for definitions of Eulerian and Lagrangian coordinates. Assuming the mapping  $\mathbf{x} + \mathbf{y}(\mathbf{x}, t)$  where

$$\mathbf{x} + \mathbf{y}(\mathbf{x}, t) = (x + y_1(x, z, t), z + y_2(x, z, t)),$$

is a diffeomorphism, then a corresponding Lagrangian averaged speed, say  $\bar{\mathbf{u}}^L(\mathbf{x}, t)$ , is defined by the equation

$$(\partial_t + \bar{\mathbf{u}}^L(\mathbf{x}, t) \cdot \nabla_{\mathbf{x}}) (\mathbf{x} + \mathbf{y}(\mathbf{x}, t)) = \mathbf{u}(\mathbf{x} + \mathbf{y}(\mathbf{x}, t), t). \quad (3.1)$$

The other requirements in the GLM formalism are that

$$\begin{aligned}\overline{\mathbf{y}(\mathbf{x}, t)} &= \mathbf{0}, \\ \overline{\mathbf{u}^L(\mathbf{x}, t)} &= \mathbf{u}^L(\mathbf{x}, t).\end{aligned}$$

These assumptions ensure that if we propagate a point  $\mathbf{x}(t)$  with the Lagrangian mean speed  $\mathbf{u}^L$ , thus making  $\mathbf{x}(t)$  a point traveling with the mean flow, then the point  $\mathbf{x}(t) + \mathbf{y}(\mathbf{x}(t), t)$  is guaranteed to be on a streamline. Using the above definitions, the Stokes drift,  $\varphi^S(\mathbf{x}, t)$ , of a quantity  $\varphi$  can be unambiguously defined to be

$$\varphi^S(\mathbf{x}, t) = \overline{\varphi}^L(\mathbf{x}, t) - \overline{\varphi(\mathbf{x}, t)}.$$

Throughout the remainder of this paper, the Eulerian average will be given by integration with respect to the fast phase variable  $\theta$ , i.e.

$$\bar{f}(\xi, z, \tau) = \frac{1}{2\pi} \int_0^{2\pi} d\theta f(\xi, z, \tau, \theta).$$

Having chosen the averaging operator, one should read the requirement  $\bar{\mathbf{y}} = 0$  as in effect a definition of the disturbance. Equation (2.23) and the definition

$$u(\mathbf{x}, t) = \omega z + \epsilon \tilde{\phi}_x(\mathbf{x}, t) + \mathcal{O}(\epsilon^3),$$

establish that

$$\overline{\phi_x} = \mathcal{O}(\epsilon^2).$$

since there are no mean terms at this order and we average over  $\theta$ .

Thus, the Eulerian mean of the horizontal velocity,  $u(\mathbf{x}, t)$ , is

$$\bar{u}(\mathbf{x}, t) = \omega z + \mathcal{O}(\epsilon^3).$$

Correspondingly, we define the Eulerian horizontal fluctuation speed  $u'(\mathbf{x}, t)$  to be

$$u'(\mathbf{x}, t) = \epsilon (e^{i\theta} R_1 + e^{-i\theta} R_1^*) + \epsilon^2 (e^{2i\theta} R_2 + e^{-2i\theta} R_2^*) + \mathcal{O}(\epsilon^3),$$

so that

$$u(\mathbf{x}, t) = \omega z + u'(\mathbf{x}, t) + \mathcal{O}(\epsilon^3).$$

It is then consistent to suppose that the disturbance  $\mathbf{y} = \mathcal{O}(\epsilon)$ , so that, with a slight abuse in notation, we have

$$\begin{aligned}\bar{u}^L(\mathbf{x}, t) &= \overline{u(\mathbf{x} + \epsilon \mathbf{y}, t)}, \\ &= \overline{\omega(z + \epsilon y_2) + u'(\mathbf{x}, t) + \epsilon(y_1(\partial_x u' + \epsilon \omega \partial_x y_2) + y_2 \partial_z u') + \mathcal{O}(\epsilon^3)}, \\ &= \omega z + \overline{\epsilon(y_1(\partial_x u' + \epsilon \omega \partial_x y_2) + y_2 \partial_z u')} + \mathcal{O}(\epsilon^3).\end{aligned}\tag{3.2}$$

Note, in order to derive the above formulas, we used a slight modification of the standard GLM transformation in which we used in the shear term  $\omega z$  the transformation

$$\omega(z + \epsilon y_2(x + \epsilon y_1, z, t)) = \omega(z + \epsilon y_2) + \epsilon^2 \omega y_1 \partial_x y_2 + \mathcal{O}(\epsilon^3).$$

This modification accounts for horizontal disturbances at or near the surface of the fluid introduced by the  $\mathcal{O}(1)$  shear current. A justification for this modification is provided at the end of this section and further corroborated by our numerical results presented in the next section. Using the definition of the SDV then gives the formula

$$u^S = \bar{u}^L - \bar{u} = \overline{\epsilon(y_1(\partial_x u' + \epsilon \omega \partial_x y_2) + y_2 \partial_z u')} + \mathcal{O}(\epsilon^3).$$

Using identical arguments for the vertical velocity  $w(\mathbf{x}, t)$  gives

$$w(\mathbf{x}, t) = w'(\mathbf{x}, t) + \bar{w}_i(\mathbf{x}, t),$$

where

$$w'(\mathbf{x}, t) = \epsilon \left( e^{i\theta} \tilde{R}_1 + e^{-i\theta} \tilde{R}_1^* \right) + \epsilon^2 \left( e^{2i\theta} \tilde{R}_2 + e^{-2i\theta} \tilde{R}_2^* \right) + \mathcal{O}(\epsilon^3),$$

and

$$\bar{w}_i = \mathcal{O}(\epsilon^3).$$

Therefore, the vertical SDV,  $w^S$ , is given by

$$w^S = \epsilon \overline{(y_1 \partial_x w' + y_2 \partial_z w')} + \mathcal{O}(\epsilon^3).$$

In order to then determine the disturbance  $\mathbf{y}$ , we note that Equation (3.1) establishes that

$$\partial_t \mathbf{y} + \omega z \partial_x \mathbf{y} - \omega \begin{pmatrix} y_2 \\ 0 \end{pmatrix} = \begin{pmatrix} R_1 e^{i\theta} + R_1^* e^{-i\theta} \\ \tilde{R}_1 e^{i\theta} + \tilde{R}_1^* e^{-i\theta} \end{pmatrix} + \mathcal{O}(\epsilon).$$

Treating the value  $z$  as an Eulerian parameter so that it is independent of time, the method of characteristics gives

$$\begin{aligned} y_1 &= -\frac{i}{k_0 \omega z + \Omega} (R_1 e^{i\theta} - R_1^* e^{-i\theta}) - \frac{\omega}{(k_0 \omega z + \Omega)^2} (\tilde{R}_1 e^{i\theta} + \tilde{R}_1^* e^{-i\theta}), \\ y_2 &= -\frac{i}{k_0 \omega z + \Omega} (\tilde{R}_1 e^{i\theta} - \tilde{R}_1^* e^{-i\theta}). \end{aligned}$$

We then use the leading order expansions

$$R_1 \sim -s\Omega\eta_1 e^{|k_0|z}, \quad \tilde{R}_1 \sim i\Omega\eta_1 e^{|k_0|z},$$

so that we get

$$\begin{aligned} y_1 &\sim \frac{-i}{k_0 \omega z + \Omega} \left( \frac{\omega \Omega}{k_0 \omega z + \Omega} - s\Omega \right) (\eta_1 e^{i\theta} - \eta_1^* e^{-i\theta}) e^{|k_0|z}, \\ y_2 &\sim \frac{\Omega}{k_0 \omega z + \Omega} (\eta_1 e^{i\theta} + \eta_1^* e^{-i\theta}) e^{|k_0|z}, \\ \partial_x u' &\sim -i\epsilon |k_0| \Omega (\eta_1 e^{i\theta} - \eta_1^* e^{-i\theta}) e^{|k_0|z}, \\ \partial_x w' &\sim -\epsilon k_0 \Omega (\eta_1 e^{i\theta} + \eta_1^* e^{-i\theta}) e^{|k_0|z}. \end{aligned}$$

Putting these terms together, and using the irrotationality of the Eulerian fluctuation speed, then gives the horizontal component of the SDV to be

$$u^S(x, z, t) = \frac{2\epsilon^2 \Omega^2}{c_p - \omega z} \left( 1 + \left( \frac{\omega}{|k_0|(c_p - \omega z)} + 1 \right)^2 \right) |\eta_1(\xi, \tau)|^2 e^{2|k_0|z} + \mathcal{O}(\epsilon^3), \quad (3.3)$$

where the phase speed  $c_p$  is given by

$$c_p(k_0, \omega) = -\frac{\Omega_{\pm}(k_0, \omega)}{k_0}.$$

Again, due to our choice of signs in  $\theta(x, t)$ , we use the opposite sign on the phase speed so that a positive phase speed  $c_p$  corresponds to a rightward propagating phase. Using similar arguments and expansions, one can show that

$$w^S = \mathcal{O}(\epsilon^3).$$

Therefore, we ignore the vertical component of the SDV throughout the remainder of this paper.

In the case of a plane-wave solution, the leading-order SDV at the surface can be evaluated in closed form giving

$$u^S(x, z, t) = \frac{2\epsilon^2 A^2 \Omega^2}{c_p - \omega z} \left( 1 + \left( \frac{\omega}{|k_0|(c_p - \omega z)} + 1 \right)^2 \right) e^{2|k_0|z} + \mathcal{O}(\epsilon^3). \quad (3.4)$$

This expands on the classic result for the SDV over infinitely deep water, and shows how constant shear currents modify the drift velocity. If the vorticity is assumed to be zero in Equation (3.4) then the classic result

$$u^S(x, z, t) = 4\epsilon^2 A^2 k_0 \sqrt{|k_0|(1 + \tilde{\sigma} k_0^2)} e^{2|k_0|z}, \quad (3.5)$$

is obtained for right-moving waves. Equation (3.4) likewise provides support for the phenomenological choices of how the SDV of a Stokes wave varies in depth made in Breivik *et al.* (2014). There, the classic formula for the SDV was modified by multiplying it by terms like  $1/(1 + \tilde{c}z)$ , where  $\tilde{c}$  was then chosen to improve agreements with observed data. Thus our result provides a physical motivation for the appearance of such terms. However, while we can put forth a physical mechanism, whether unresolved shear currents near the surface are truly responsible for disagreements between theory and observation is a matter for future work.

Since we are most interested in surface dynamics, in which  $z = \epsilon\eta(x, t)$ , we can then use  $z \sim 0$ , so that the SDV for the Jacobi elliptic function solutions with  $\beta = 1$  is given by

$$u^S(x, 0, t) = -4\epsilon^2 \kappa^2 k_0 \Omega \left| \frac{\alpha_d}{\alpha_{nl}} \right| \left( 1 + \left( 1 - \frac{s\omega}{\Omega} \right)^2 \right) \phi(\xi; \kappa),$$

where

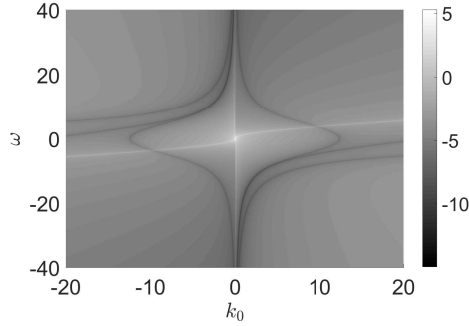
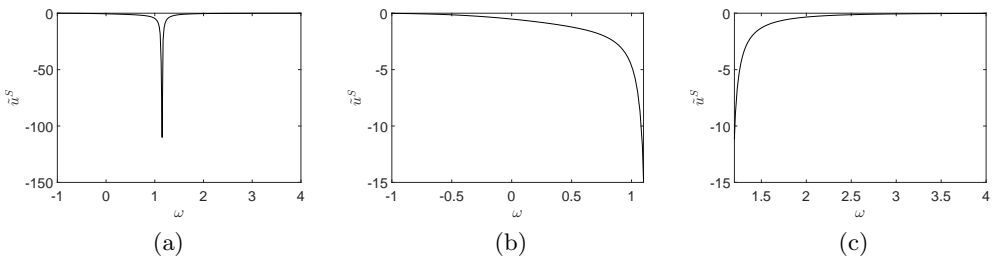
$$\phi(\xi; \kappa) = \begin{cases} \text{cn}^2(\xi; \kappa), & \alpha_d/\alpha_{nl} > 0, \\ \text{sn}^2(\xi; \kappa), & \alpha_d/\alpha_{nl} < 0. \end{cases}$$

Defining the parameter

$$\tilde{u}^S(k_0, \omega) = -4k_0 \Omega(k_0, \omega) \left| \frac{\alpha_d(k_0, \omega)}{\alpha_{nl}(k_0, \omega)} \right| \left( 1 + \left( 1 - \frac{s\omega}{\Omega(k_0, \omega)} \right)^2 \right),$$

and choosing the positive branch of the dispersion relationship, Figure 2 shows that this term exhibits a wide variation in magnitude. The curves along which the largest magnitudes are seen correspond to the level set  $\alpha_{nl}(k_0, \omega) = 0$ . Thus, for the class of Jacobi elliptic solutions, there appears to be a kind of nonlinear resonance between the shear current and the carrier wave. We point out that along this curve though, the assumptions we used to derive the NLS equation are no longer valid. Therefore, more work should be done to better elucidate the affiliated dynamics associated with parameter choices defining said curve. Throughout the remainder of this paper, we choose parameter values that do not place us too near the zero set of  $\alpha_{nl}(k_0, \omega) = 0$ .

To get a more detailed understanding of how the SDV depends on the shear current strength, we choose  $k_0 = 1$  and use the positive branch of the dispersion relationship. Figure 3 contains plots of  $\tilde{u}^S(1, \omega)$  for  $-1 \leq \omega \leq 4$ ,  $-1 \leq \omega \leq 1.1$ , and  $1.2 \leq \omega \leq 4$ . We choose these particular ranges of shear values to in particular examine the behavior of  $\tilde{u}^S$  around the resonance curve seen in Figure 2. The singularity seen in Figure 3 (a) corresponds to the value  $\omega$  such that  $\alpha_{nl}(1; \omega) = 0$ , namely  $\omega \approx 1.1550$ . Figure 3 (b)

FIGURE 2. Plot of  $\log_{10} |\tilde{u}^S(k_0, \omega)|$ .FIGURE 3. Plots of  $\tilde{u}^S(1, \omega)$  choosing  $\Omega_+(1, \omega)$  as the choice of the dispersion relationship for  $-1 \leq \omega \leq 4$  (a),  $-1 \leq \omega \leq 1.12$  (b), and  $1.17 \leq \omega \leq 4$  (c). Note,  $\alpha_{nl}(1; 1.1550) = 0$ . The figure then shows that the magnitude of the SDV increases with increasing shear on the focusing side of the singularity (b), and decreases with increasing shear on the defocusing side (c).

shows the focusing side and that increasing the shear strength increases the Stokes drift velocity. Figure 3 (c) shows that this relationship is reversed on the defocusing side.

Next, we address the question of the Lagrangian drift velocity (LDV)  $\bar{u}^L(x, z, t)$  at or near the surface  $z = \epsilon\eta$ . Using Equation (2.9) for the mean surface displacement term  $\eta_0$ , Equation (3.3) for the SDV, and Equation (3.2) for  $\bar{u}^L$ , the leading-order LDV at the surface  $z = \epsilon\eta$ , say  $\bar{u}^{L,s}(x, t)$ , is given by

$$\bar{u}^{L,s}(x, t) = \epsilon^2 u_p^L(k_0, \omega) |\eta_1(\xi, \tau)|^2 + \mathcal{O}(\epsilon^3),$$

where the scaling factor  $u_p^L$  is given by

$$u_p^L(k_0, \omega) = \frac{\omega^2(2s\Omega(k_0, \omega) - \omega)}{1 + \omega c_g(k_0, \omega)} - 2k_0\Omega(k_0, \omega) \left( 1 + \left( 1 - \frac{s\omega}{\Omega(k_0, \omega)} \right)^2 \right).$$

The LDV determines the mean horizontal velocity of a particle at or near the surface, and this is then controlled by the magnitude of the solution to the NLS equation we study and the magnitude of  $u_p^L$ . Of particular interest given the puzzling results on the existence of drift quenching Eulerian counterflows Monismith *et al.* (2007); Smith (2006), we can also then determine vorticity values  $\omega$  for a given wavenumber  $k_0$  such that  $u_p^L(k_0, \omega) = 0$ , which corresponds to the presence of an Eulerian counterflow which counters the effect of the SDV. We plot this zero level set for  $0 \leq k_0 \leq 20$  in Figure 4. As can be seen, shear strengths which contribute to the suppression of particle drift are always counter-propagating relative to a positively elevated surface.

At this point, we note that had we not introduced the modification to GLM used

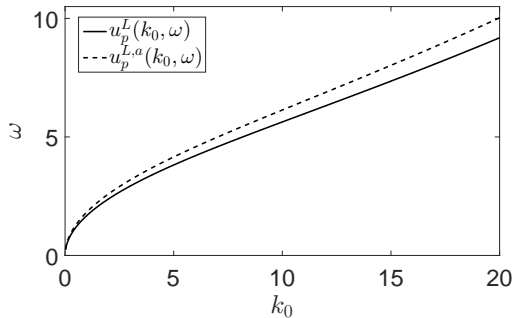


FIGURE 4. Plot of the zero sets  $u_p^L(k_0, \omega) = 0$  and  $u_p^{L,a}(k_0, \omega) = 0$ .

above, the formula we would get for the LDV at the surface, say  $u_p^{L,a}$  would be

$$u_p^{L,a}(k_0, \omega) = \frac{\omega^2(2s\Omega(k_0, \omega) - \omega)}{1 + \omega c_g(k_0, \omega)} - 2k_0\Omega(k_0, \omega) \left( 2 - \frac{s\omega}{\Omega(k_0, \omega)} \right).$$

As one would expect, our modification of the GLM approach alters the computation of the SDV, which in turn then would markedly shift where the zero set of  $u_p^{L,a}(k_0, \omega)$  appears relative to the zero set of  $u_p^L(k_0, \omega)$ . This is illustrated by comparing the two curves plotted in Figure 4. As shown in subsequent sections, the numerical simulations we have developed confirm the prediction of quenched surface drift velocity given by finding  $u_p^L(k_0, \omega) = 0$ , thereby validating our generalization of the GLM methodology.

#### 4. Numerical Results

In order to determine the particle paths, the system in Equation (2.16) must be solved. However, since the NLS solutions are in terms of the coordinates  $\xi$  and  $\tau$ , the dynamical system

$$\begin{aligned} \frac{d\xi_s}{d\tau} &= \frac{c_g}{\epsilon} + \frac{\omega}{\epsilon} z_s + \tilde{\phi}_x(\xi_s, z_s), & \frac{dz_s}{d\tau} &= \frac{1}{\epsilon} \tilde{\phi}_z(\xi_s, z_s), \\ \xi_s(0) &= \xi_0, & z_s(0) &= z_0, \end{aligned}$$

where the potentials  $\tilde{\phi}_x$  and  $\tilde{\phi}_z$  are found in Equations (2.23) and (2.24) respectively must be solved. Given our focus on determining particle paths at the surface, we approximate the surface profile by

$$z_s(t) = \epsilon \tilde{\eta}(\xi_s(t), t).$$

Thus, the coupled system of ODEs is reduced to a single, nonlinear, scalar equation

$$\begin{aligned} \frac{d\xi_s}{d\tau} &= \frac{c_g}{\epsilon} + \omega \tilde{\eta}(\xi_s, t) + \tilde{\phi}_x(\xi_s, \epsilon \tilde{\eta}), \\ \xi_s(0) &= \xi_0. \end{aligned}$$

We use a fourth-order Runge-Kutta scheme with a time step of  $\delta\tau = 5 \times 10^{-4}$  to solve this initial-value problem.

For the Jacobi elliptic function solutions, we choose the initial tracer position to be

$$\xi_s(0) = \frac{K(\kappa)}{128}, \quad z_s(0) = \epsilon \tilde{\eta}(\xi_s(0), 0),$$

where  $K(\kappa)$  is the complete elliptic integral of the first kind and  $\tilde{\eta}$  is defined by Equation

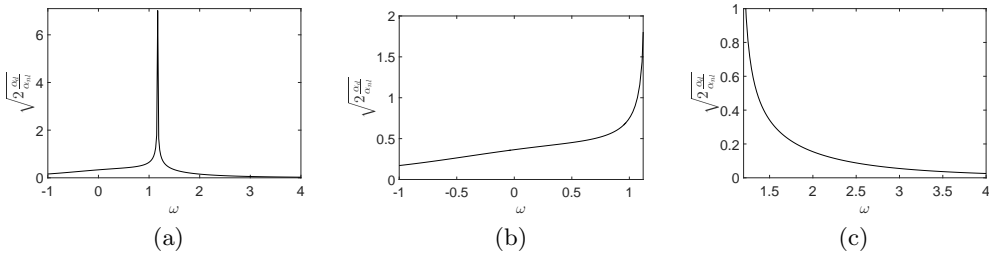


FIGURE 5. Plots of  $\sqrt{2|\alpha_d/\alpha_{nl}|}$  for  $k_0 = 1$  and  $\Omega_+$  as the choice of the dispersion relationship for  $-1 \leq \omega \leq 4$  (a),  $-1 \leq \omega \leq 1.12$  (b), and  $1.17 \leq \omega \leq 4$  (c).

(2.6). For the plane wave solutions, we chose  $\xi_s(0) = 10/128$  so the initial positions are comparable across the different classes of solutions. We take the positive branch of the dispersion relationship, which implies that  $k_0 > 0$  corresponds to a left-moving-carrier wave. We choose  $k_0 = 1$  for the plane-wave solutions. In the case of the Jacobi elliptic solutions to the NLS equation, we choose the integer  $m$  to be

$$m = \left\lfloor \frac{2K(\kappa)}{\pi\epsilon} \right\rfloor,$$

so that, using Equation (2.13),  $k_0 \approx 1$ . In practice,  $k_0 \approx 0.98$  or  $0.99$ . The results for the tracer position in physical coordinates,  $(x_s(t), z_s(t))$ , are found using the transformations

$$x_s(t) = \frac{\xi_s(\tau)}{\epsilon} - \frac{c_g\tau}{\epsilon^2}, \quad t = \frac{\tau}{\epsilon^2}.$$

Fourier transforms and their inverses are computed numerically using the fast Fourier transform.

Finally, note that the expansions in (2.23) and (2.24), and the associated approximations in (2.25) and (2.26), show that the strength of the velocity field is largely determined by the magnitude of the solution to the NLS equation given by  $\eta_1$ . In the case of the Jacobi elliptic function solutions, controlling for the elliptic modulus  $\kappa$ , the term  $\sqrt{2|\alpha_d/\alpha_{nl}|}$  is the most significant contribution to the magnitude of  $\eta_1$  since we have fixed  $\beta = 1$ ; see Equations (2.11) and (2.12). Figure 5 contains plots of  $\sqrt{2|\alpha_d/\alpha_{nl}|}$  versus  $\omega$  for  $k_0 = 1$ . In the focusing case, increasing the magnitude of the Jacobi elliptic function solutions corresponds to increasing the shear strength. In the defocusing case, decreasing the magnitude of the Jacobi elliptic function solutions corresponds to increasing the shear strength. These two statements are justified by the similarities of Figures 5 (b) and (c) and 3 (b) and (c). Therefore, relatively large amplitude solutions inducing strong fluid particle drift is to be expected near the resonance curve.

#### 4.1. Focusing Case

Using the solution given in equation (2.11) with  $k_0 \approx 1$  ensures that  $\omega = 0$  and  $\omega = \pm 1$  are in the focusing regime. Figure 6 shows the paths of particles for three values of  $\omega$  found by setting  $\epsilon = 0.1$ ,  $\kappa = 0.5$ , and solving the dynamical system for the particle paths up to time  $t = 1/\epsilon^2$ . The carrier profile is propagating to the left in this situation. Therefore, if  $\omega = 1.12$ , then the shear current is counter-propagating at the surface with respect to the carrier wave while if  $\omega = -1$ , the current is co-propagating. The counter-propagating current significantly enhances the leftward horizontal motion of a tracer along the surface as seen by comparing Figures 6(b) and (c) with (a). This can be

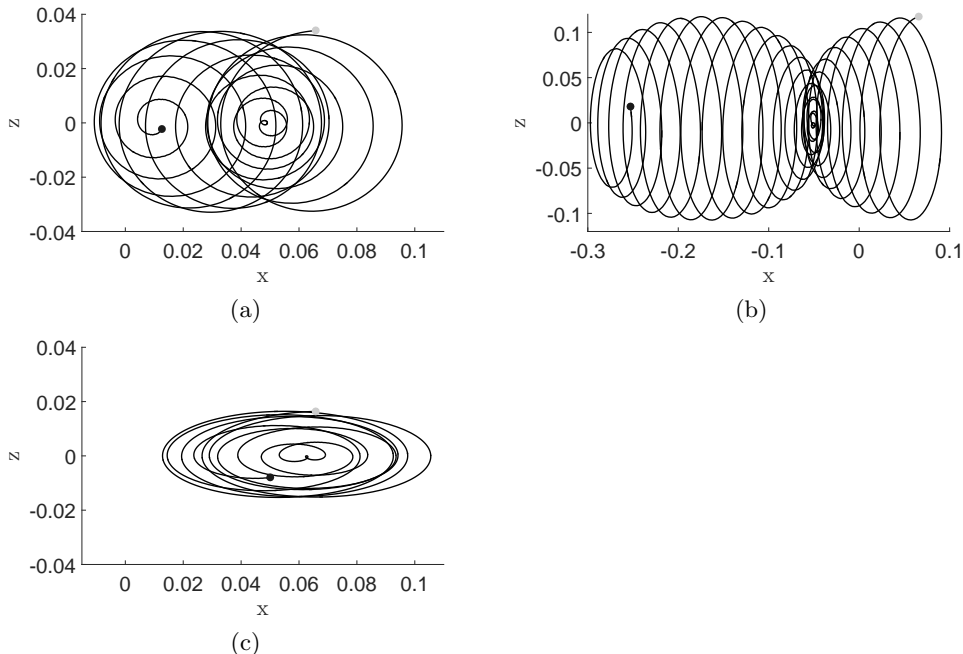


FIGURE 6. **Focusing Case** - Plots of particle paths correspond to the solution given in Equation (2.11) with  $\epsilon = 0.1$ ,  $\beta = 1$ ,  $k_0 \approx 1$ ,  $\kappa = 0.5$ , with  $\omega = 0$  (a),  $\omega = 1.12$  (b), and  $\omega = -1$  (c). The grey dots indicate the starting positions of the tracers while the black dots indicate their final positions.

explained by examining the values of the SDV and the LDV parameters

$$\begin{aligned} \tilde{u}^S(1, 0) &= -0.5179, & \tilde{u}^L(1, 0) &= -0.5179, \\ \tilde{u}^S(1, 1.12) &= -10.5051, & \tilde{u}^L(1, 1.12) &= -5.1109, \\ \tilde{u}^S(1, -1) &= -0.2779, & \tilde{u}^L(1, -1) &= -0.1601, \end{aligned}$$

where the parameter  $\tilde{u}^L$  is defined to be

$$\tilde{u}^L(k_0, \omega) = 2 \left| \frac{\alpha_d(k_0, \omega)}{\alpha_{nl}(k_0, \omega)} \right| u_p^L(k_0, \omega).$$

Note that for the Jacobi elliptic solutions and controlling for  $\kappa$  and  $\beta$ , this will be the most significant contribution to the magnitude of the LDV. This demonstrates why the counter-propagating current so enhances the leftward drift since the LDV parameter is an order of magnitude larger than in the other cases. Further, it demonstrates why the co-propagating current, i.e.  $\omega = -1$ , reduces the horizontal displacement of the surface particle. This is somewhat surprising as one might intuitively imagine that the co-propagating shear would enhance the particle drift, especially in comparison to the zero vorticity case. However, we have effectively shown that nonlinearity makes the surface/current interaction a more complicated one than one might at first suspect.

Choosing  $\kappa = 0.99$  shows that similar results hold closer to the solitary wave solution; see Figure 7, though the larger elliptic modulus results in the larger amplitudes and leftward drifts. In particular, near the solitary wave limit, positive, counter-propagating shear can greatly enhance both the impact of nonlinearity and the transport properties of the waves.



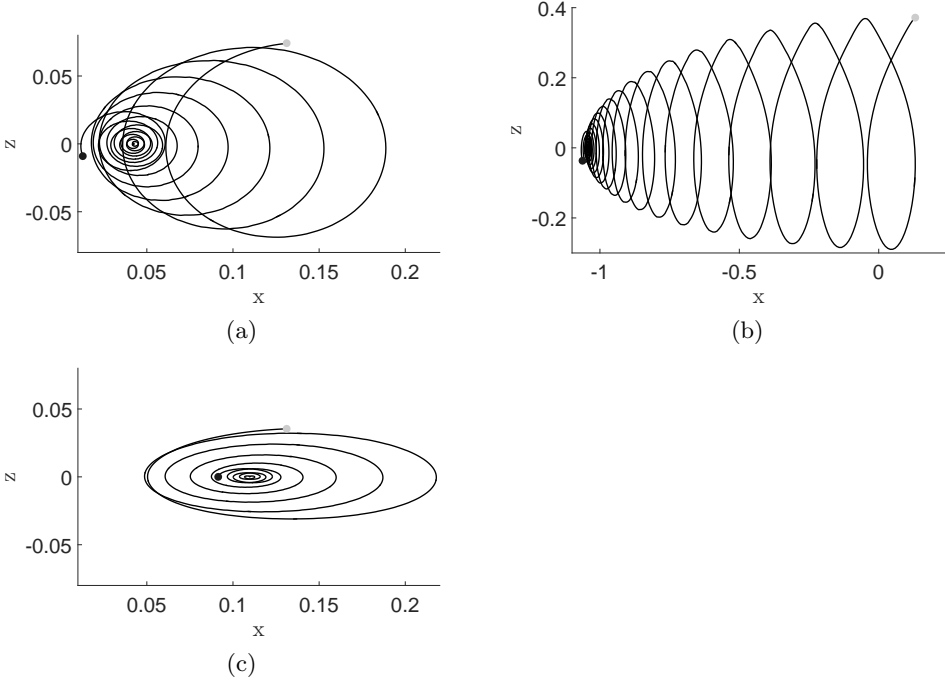


FIGURE 7. **Focusing Case** - Plots of particle paths correspond to the solution given in Equation (2.11) with  $\epsilon = 0.1$ ,  $\beta = 1$ ,  $k_0 \approx 1$ ,  $\kappa = 0.99$ , with  $\omega = 0$  (a),  $\omega = 1.12$  (b), and  $\omega = -1$  (c). The grey dot indicates the starting position of the tracer while the black dot indicates the final position.

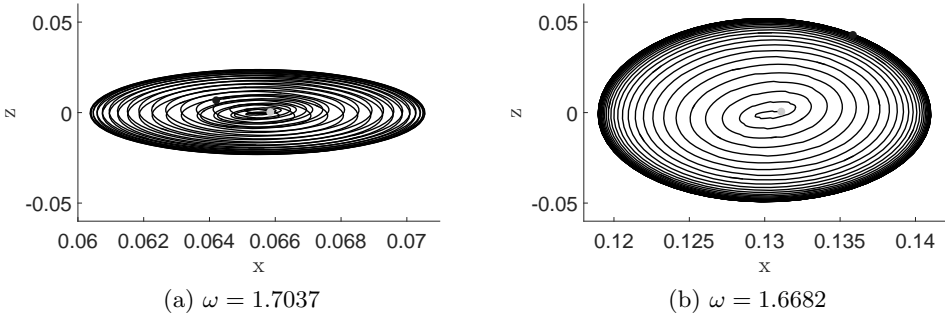


FIGURE 8. **Defocusing Case** - Plots of particle paths correspond to the solution given in Equation (2.12) with  $\epsilon = 0.1$ ,  $\beta = 1$ ,  $k_0 \approx 1$ , with  $\kappa = 0.5$  (a),  $\kappa = 0.99$  (b). The grey dots indicate the starting positions of the tracers while the black dots indicate their final positions.

#### 4.2. Defocusing Case

For the Jacobi elliptic solutions with  $k_0 \approx 1$ , the zero LDV solutions belong in the defocusing case. Figure 8 shows the impact on surface flow particle paths when  $\omega$  is chosen to zero out the LDV. As can be seen, the particle paths, while not exactly closed, are spirals and are constrained in their horizontal and vertical extent by an outer elliptical perimeter. Similarly, the shear strength can be chosen so that the LDV is zeroed out for the plane-wave solutions. Taking  $k_0 = 1$  and  $A = 1$ , this corresponds to choosing  $\omega = 1.6828$ . Figure 9 shows a nearly closed particle path. We emphasize that these results are a confirmation of the predictions made in Figure 4. Thus, these numerical results

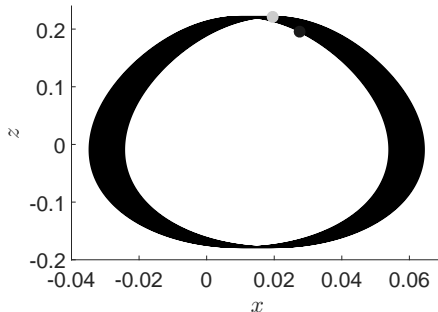


FIGURE 9. **Defocusing Case** - Plot of a particle path corresponding to a plane-wave solution with  $\epsilon = 0.1$ ,  $A = 1$ ,  $k_0 = 1$ , and  $\omega = 1.6828$ , which ensures that  $\tilde{u}^L(1, \omega) = 0$ , thereby leading to the nearly closed particle path.

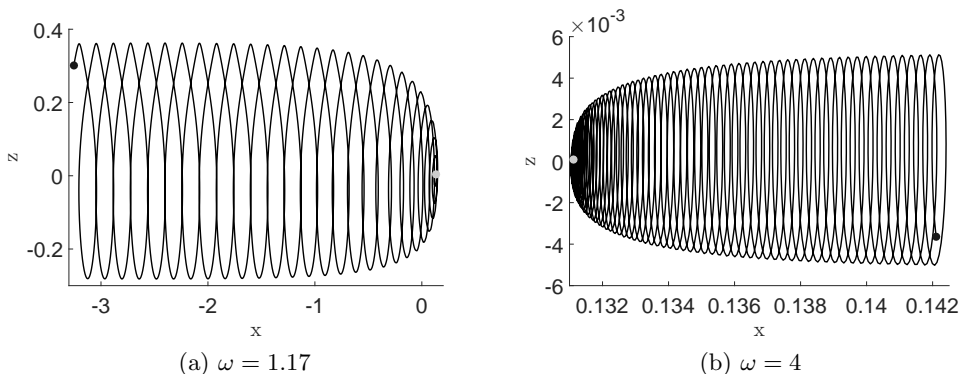


FIGURE 10. **Defocusing** - Near dark soliton solution for  $k_0 \approx 1$ ,  $\kappa = .99$  and  $\omega = 1.17$  (a) and  $\omega = 4$  (b). The grey dot indicates the starting position of the tracer while the black dot indicates the final position.

validate our choice to generalize the GLM approach in so far as we see the generalization provides the correct predictions for when shear will quench surface drift.

In some respects then, we have also shown that by appropriately choosing the shear, we can replicate the dynamics of a Gerstner wave Constantin (2011) by looking instead at a plane-wave moving over a counter-propagating shear current. This could point towards resolving some of the questions raised in Monismith *et al.* (2007); Smith (2006), though this is a subject of future research.

Looking beyond cases in which Eulerian counterflows quench drift, we now consider the defocusing NLS Jacobi elliptic function solutions given in Equation (2.12). We choose  $k_0 \approx 1$ ,  $\epsilon = 0.1$ ,  $\kappa = 0.99$  (near the dark-soliton limit). Solving the dynamical system for the particle paths up to time  $t = 1/\epsilon^2$  generates Figure 10 (a) and (b) for  $\omega = 1.17$  and  $\omega = 4$  respectively. While the particle path motion seen in Figure 10(a) is rapidly oscillating, the net transport and amplitude is quite small.

However, if  $\omega = 4$  in the case of a plane wave, we do not necessarily get the same diminished response seen for the Jacobi elliptic solutions; see Figure 11. The highly oscillatory plane wave profile induces a particle path which ultimately exhibits a strong rightward drift which follows the strong counter-propagating shear current. Using Equations (3.2) and (3.4), and expanding around  $z = \epsilon\eta$ , the associated SDV and

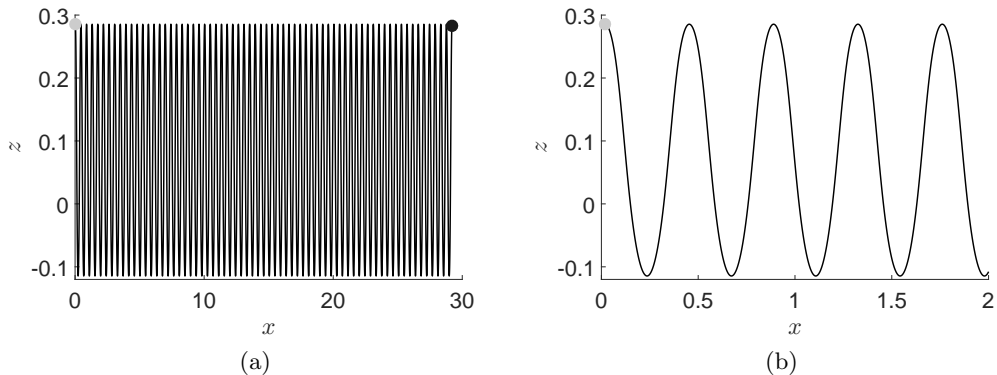


FIGURE 11. **Defocusing Case** - Plane-wave solution for  $k_0 = 1$ ,  $\omega = 4$ ,  $A = 1$ , with (b) providing a detail of (a). The grey dot indicates the starting position of the tracer while the black dot indicates the final position.

LDV at the surface for the plane wave with these parameters are given by

$$\begin{aligned} u^S &= -8.9452\epsilon^2 + \mathcal{O}(\epsilon^3), \\ \bar{u}^L &= 28.7778\epsilon^2 + \mathcal{O}(\epsilon^3). \end{aligned}$$

This explains the stronger net rightward drift of the particle shown in Figure 11. Finally, note that this shows the SDV and the LDV can oppose one another, thereby clarifying the need to use both velocities to fully understand the drift properties associated with a surface wave.

## 5. Acknowledgments

This material is based upon work supported by the National Science Foundation under Grant No. DMS-1439786 while CWC and JDC were in residence at the Institute for Computational and Experimental Research in Mathematics in Providence, RI, during the Spring 2017 semester. Additionally, JDC acknowledges and thanks the Norwegian Fulbright Core Scholar Program for supporting his five-month long visit to the University of Bergen to work with HK. This research was also supported by the Research Council of Norway through grants 213474/F20 and 239033/F20.

## REFERENCES

- ABLOWITZ, M.J., FOKAS, A.S. & MUSSLIMANI, Z.H. 2006 On a new non-local formulation of water waves. *J. Fluid Mech.* **562**, 313–343.
- ANDREWS, D.G. & MCINTYRE, M.E. 1978 An exact theory of nonlinear waves on a Lagrangian-mean flow. *J. Fluid Mech.* **89**, 609–646.
- ASHTON, A.C.L. & FOKAS, A.S. 2011 A non-local formulation of rotational water waves. *J. Fluid Mech.* **689**, 129–148.
- BAUMSTEIN, A.I. 1998 Modulation of gravity waves with shear in water. *Stud. Appl. Math.* **100**, 365–390.
- BORLUK, H. & KALISCH, H. 2012 Particle dynamics in the KdV approximation. *Wave Motion* **49**, 691–709.
- BREIVIK, Ø., JANSSEN, P.A.E.M. & BIDLOT, J.R. 2014 Approximate Stokes drift profiles in deep water. *J. Phys. Ocean.* **44**, 2433–2445.
- BREVIK, I. 1979 Higher-order waves propagating on constant vorticity currents in deep water. *Coastal Eng.* **2**, 237–259.

- BÜHLER, O. 2009 *Waves and Mean Flows*. Cambridge: Cambridge.
- CHOI, W. 2009 Nonlinear surface waves interacting with a linear shear current. *Math. Comput. Simul.* **80**, 101–110.
- CONSTANTIN, A. 2011 *Nonlinear Water Waves with Applications to Wave-Current Interactions and Tsunamis*. Philadelphia, P.A.: SIAM.
- FOKAS, A.S. 2008 *A Unified Approach to Boundary Value Problems*. Philadelphia, PA: SIAM.
- FOLLAND, G. 1999 *Real Analysis: Modern Techniques and Their Applications*. New York, NY: Wiley.
- GALLET, B. & YOUNG, W.R. 2014 Refraction of swell by ocean currents. *J. Mar. Res.* **72**, 105–126.
- HELFRICH, K.R. & MELVILLE, W.K. 2006 Long nonlinear internal waves. *Ann. Rev. Fluid Mech.* **38**, 395–425.
- JR, R. RIBEIRO, MILEWSKI, P.A. & NACHBIN, A. 2017 Flow structure beneath rotational water waves with stagnation points. *J. Fluid Mech.* **812**, 792–814.
- KUNDU, P.K., COHEN, I.M. & DOWLING, D.R. 2012 *Fluid Mechanics*, 5th edn. New York, N.Y.: Elsevier.
- LONGUET-HIGGINS, M.S. 1953 Mass transport in water waves. *Phil. Trans. Roy. Soc. Lond.* **245**, 535–581.
- MCWILLIAMS, J.C., SULLIVAN, P.P. & MOENG, C.H. 1997 Langmuir turbulence in the ocean. *J. Fluid Mech.* **334**, 1–30.
- MONISMITH, S.G., COWEN, E.A., NEPF, H.M., MAGNAUDET, J. & THAIS, L. 2007 Laboratory observations of mean flows under surface gravity waves. *J. Fluid Mech.* **573**, 131–147.
- SIMMEN, J.A. & SAFFMAN, P.G. 1985 Steady deep-water waves on a linear shear current. *Stud. Appl. Math.* **75**, 35–57.
- SMITH, J.A. 2006 Observed variability of ocean wave Stokes drift, and the Eulerian response to passing groups. *J. Phys. Oceanogr.* **36**, 1381–1402.
- THOMAS, R., KHARIF, C. & MANNA, M. 2012 A nonlinear Schrödinger equation for water waves on finite depth with constant vorticity. *Phys. Fluids* **24** (12), 127102.
- WEBB, A. & FOX-KEMPER, B. 2011 Wave spectral moments and Stokes drift estimation. *Ocean Model.* **40**, 273–288.